

# Observations and modeling of the Mars low-altitude ionospheric response to the September 10, 2017 X-Class solar flare

Shaosui Xu<sup>1</sup>, Ed Thiemann<sup>2</sup>, David Mitchell<sup>1</sup>, Frank Eparvier<sup>2</sup>, David Pawlowski<sup>3</sup>, Mehdi Benna<sup>4</sup>, Laila Andersson<sup>2</sup>, Michael W. Liemohn<sup>5</sup>, Stephen Bougher<sup>5</sup>, Christian Mazelle<sup>6</sup>

---

Shaosui Xu, shaosui.xu@ssl.berkeley.edu

<sup>1</sup>Space Sciences Laboratory, University of California, Berkeley, USA

<sup>2</sup>Laboratory for Atmospheric and Space Physics, University of Colorado, Boulder, Colorado, USA

<sup>3</sup>Physics Department, Eastern Michigan University, Ypsilanti, Michigan, USA

<sup>4</sup>NASA Goddard Space Flight Center, Greenbelt, Maryland, USA

This article has been accepted for publication and undergone full peer review but has not been through the copyediting, typesetting, pagination and proofreading process, which may lead to differences between this version and the Version of Record. Please cite this article as doi: 10.1029/2018GL078524

Solar extreme ultraviolet and X-ray photons are the main sources of ionization in the Martian ionosphere and can be enhanced significantly during a solar flare. On September 10, 2017, the Mars Atmosphere and Volatile Evolution (MAVEN) orbiter observed an X8.2 solar flare, the largest it has encountered to date. Here, we investigate the ionospheric response before, during, and after this event with the SuperThermal Electron Transport (STET) model. We find good agreement between modeled and measured photoelectron spectra. In addition, the high photoelectron fluxes during the flare provide adequate statistics to allow us to clearly and repeatedly identify the carbon Auger peak in the ionospheric photoelectron energy spectra at Mars for the first time. By applying photochemical equilibrium,  $O_2^+$  and  $CO_2^+$  densities are obtained and compared with MAVEN observations. The variations in ion densities during this event due to the solar irradiance enhancement and the neutral atmosphere expansion are discussed.

**Keypoints:**

---

<sup>5</sup>Department of Climate and Space  
Sciences and Engineering, University of  
Michigan, Ann Arbor, Michigan, USA

<sup>6</sup>IRAP, CNRS - University of Toulouse -  
UPS - CNES, Toulouse, France

- The modeled and measured photoelectron spectra are in good agreement during an X8.2 solar flare event
- The carbon Auger peak is clearly and repeatedly identified in electron energy spectra of the Martian ionosphere for the first time
- The ion density enhancement due to the flare at a fixed altitude is from tens to 1500 percent

Accepted Article

## 1. Introduction

Solar extreme ultraviolet (EUV, 10 – 100 nm) and X-ray (<10 nm) photons are the main sources of ionization in the Martian ionosphere, photoionizing the neutral atmosphere (mainly CO<sub>2</sub> and O) and creating the M2 and M1 layers at Mars, respectively [e.g. *Fox*, 2004a; *Withers*, 2009], analogous to Earth's F1 and E region [cf. *Bougher et al.*, 2017]. Many properties of the M2 layer observed by previous Mars missions [cf. *Withers*, 2009] can be explained by Chapman theory [*Chapman*, 1931a, b]. In contrast, the M1 peak is hard to reproduce without sophisticated photochemical models [e.g. *Fox*, 2004b]. The monochromatic assumption of Chapman theory fails at the M1 layer because the photoionization cross section of CO<sub>2</sub> for soft X-rays decreases rapidly with decreasing wavelength. In addition, electron impact ionization (EII) from photoelectrons becomes more important below the main (M2) peak [*Withers*, 2009]. Simulating EII can be achieved by employing either an electron transport model [e.g. *Fox and Dalgarno*, 1979] or a wavelength-dependent yield function to represent multiple ion-electron pairs being created by a single photon [e.g. *Bougher et al.*, 2001; *Mendillo et al.*, 2006; *Haider et al.*, 2012; *Lollo et al.*, 2012; *Fallows et al.*, 2015a].

Solar EUV and X-ray fluxes vary strongly with solar activity. In particular, during a solar flare, these short wavelength photons can be enhanced by a factor of a few to orders of magnitude. Photoelectrons are created during the photoionization process and transfer energy to the thermosphere and ionosphere via electron-neutral collisions and electron-electron Coulomb collisions, causing heating, ionization, and emission [e.g. *Fox and Dalgarno*, 1979]. Photoelectron energy spectra are very sensitive to solar spectral

variations [e.g. *Peterson et al.*, 2012; *Xu et al.*, 2015a; *Sakai et al.*, 2015]. *Peterson et al.* [2016] investigated how photoelectron spectra change before and after a solar flare with MAVEN measurements and simulations, including three photoelectron production models and two solar irradiance models. The variation in the solar spectrum is also reflected in ionospheric properties. *Gurnett et al.* [2005] first reported the flare induced ionospheric enhancement at and above the M2 peak with measurements from the Mars Advanced Radar for Subsurface and Ionosphere Sounding (MARSIS) onboard Mars Express. The first observation of the M1 layer's response to a solar flare was reported by *Mendillo et al.* [2006] with radio occultation measurements of electron density with the Mars Global Surveyor (MGS) spacecraft, which showed an enhancement of up to 200% in density at 90-95 km. More recently, ionospheric electron density responses to flares were investigated with MGS and Mars Express data [e.g. *Nielsen et al.*, 2007; *Mahajan et al.*, 2009; *Haider et al.*, 2009; *Fallows et al.*, 2015b, c]. There were also modeling efforts dedicated to reproducing the low-altitude ionospheric responses to flares [e.g. *Lollo et al.*, 2012; *Haider et al.*, 2012, 2016].

On September 10, 2017, MAVEN observed an X8.2 solar flare, the largest it has encountered to date. The EUV and X-ray fluxes increased by  $\sim 100\%$  (a factor of  $\sim 2$ ) and  $\sim 1000\%$  (a factor of  $\sim 11$ ), respectively, for this event. During the flare's declining phase, MAVEN was taking in-situ measurements of neutral and ion densities for multiple species with the Neutral Gas and Ion Mass Spectrometer (NGIMS) instrument [*Mahaffy et al.*, 2015], the thermal electron density and temperature with the Langmuir Probe and Waves (LPW) instrument [*Andersson et al.*, 2015], and superthermal electron fluxes with the

Solar Wind Electron Analyzer (SWEA) [Mitchell *et al.*, 2016]. Additionally, EUV irradiance measurements in three wavelength bands made by the Extreme UltraViolet Monitor (EUVM) instrument [Eparvier *et al.*, 2015] are used to drive a spectral irradiance model, providing predictions of solar irradiance from 0.1 nm to 189.5 nm [Thiemann *et al.*, 2018]. These comprehensive measurements provide an opportunity to evaluate the ionospheric response to this flare event in detail with validated numerical models, using direct measurements or measurement-constrained simulations as inputs. This study investigates the low-altitude ionospheric response to the flare, which is an important part of how the Martian environment responds to such a space weather event. To the best of our knowledge, this is also the first to compare model results directly to ion measurements.

## 2. Observations and Modeling of Photoelectrons

The ionizing 0-91 nm solar flux due to this flare increases sharply at 15:43:40 UT on September 10, 2017, reaching the peak value within  $\sim 10$  min, where it remains for  $\sim 24$  min. The flux then decays to half of its maximum after  $\sim 36$  min, and returns to the pre-flare level near the end of day [Thiemann *et al.*, 2018]. In this study, we choose three time periods to investigate this event: the periapsis pass before the flare, during the flare peak when MAVEN was at its apoapsis, and the first periapsis pass after the peak, when the flare was in its declining phase. MAVEN in situ observations of the ionosphere were obtained during both periapsis passes. The SuperThermal Electron Transport (STET) model [Khazanov and Liemohn, 1995; Liemohn *et al.*, 2003; Xu and Liemohn, 2015; Xu *et al.*, 2015a] is used to simulate photoelectron spectra and ion production rates. Around the time of the flare, MAVEN had a periapsis altitude of  $\sim 155$  km at a solar zenith angle

of 70°, which is above the M2 peak. For this event, we use neutral and plasma density and temperature measurements from MAVEN as model inputs. In order to extend simulations down to 100 km to examine the response of both the M1 and M2 layers, we adopt neutral profiles from simulation results with the Mars Global Ionosphere-Thermosphere Model (M-GITM) [Bougher *et al.*, 2015] for this event.

## 2.1. Inputs for STET Modeling

The STET model solves the gyro-averaged Boltzman equation and calculates the superthermal electron flux along a single magnetic flux tube. The cross-section information for photoionization and excitation in the Mars environment used by the STET model is from Fox [1991], with an updated electron impact cross section from Fox and Sung [2001]. See more details about the STET model in Xu and Liemohn [2015] and Xu *et al.* [2015a]. The solar spectra for these three time periods from Thiemann *et al.* [2018] are displayed in Figure 1a. The solar flux enhancement due to this flare event exhibits large, wavelength-dependent variations and is up to 1-2 orders of magnitude for wavelengths  $\lambda > 15$  nm.

Other key input profiles for the STET model include the CO<sub>2</sub> and O densities (three other neutral species, CO, N<sub>2</sub>, and O<sub>2</sub>, are also included in the model but not shown) and electron temperatures, obtained through a combination of MAVEN observations and M-GITM simulation results, which are shown in Figures 1b-1d. More specifically, for the pre-peak flare period, the O density from M-GITM is spliced directly to the NGIMS data at altitudes below periapsis, where NGIMS measurements are not available; the CO<sub>2</sub> density from M-GITM is shifted up 10 km prior to splicing with the NGIMS data (to

force the model absolute values to agree with the data). For the post-peak flare period, we shift the M-GITM CO<sub>2</sub> density up 15 km and the M-GITM O density up 9 km prior to splicing with the NGIMS data. Neutral density enhancements at a fixed altitude are due to heating of the thermosphere during the flare [e.g. *Qian et al.*, 2011; *Thiemann et al.*, 2015]. Finally, for the electron temperature ( $T_e$ ) profiles, we use the M-GITM CO<sub>2</sub> profiles below 115 km to estimate the lower thermosphere temperature and linearly extrapolate the LPW measured  $T_e$  to the neutral temperature at low altitudes, an approach adopted by previous studies [e.g. *Mendillo et al.*, 2011]. Below 115 km, collisions between neutrals and charged particles are so frequent that the electron temperature is expected to be similar to the neutral temperature. A solar zenith angle (SZA) of 70° is used in all simulations, which corresponds with MAVEN's periapsis location for these two orbits.

Because the flare peaks when MAVEN was near apoapsis, far above the ionosphere, we combine density and temperature profiles from the periapsis pass before the peak with the solar spectrum at the peak to simulate the ionospheric response to the peak flare irradiance. Because the flare irradiance peaks rapidly (within ~10 min) [*Thiemann et al.*, 2018] and the thermospheric response is expected to lag that of the ionosphere [e.g. *Thiemann et al.*, 2015], the pre-flare density profiles better represent the peak-flare period. This also allows us to isolate the ionospheric response solely to solar flux variations.

## 2.2. Data-Model Comparison of Photoelectron Spectra

The modeled photoelectron spectra at 155 km, convolved with SWEA's energy response function [*Mitchell et al.*, 2016], for the pre-peak, peak, and post-peak flare periods are shown with black, red, and blue thin lines, respectively, in Figure 2a. The spacecraft

potential is near  $-2.5$  V for both the pre-flare and post-peak flare periapses. This potential is applied to the modeled spectra as follows: the modeled spectra in units of differential energy flux ( $\text{eV}/\text{cm}^2\text{-sec-ster-eV}$ ) are first converted to phase space density ( $\text{cm}^{-3} (\text{cm}/\text{s})^{-3}$ ), where they are shifted in energy by  $2.5$  eV, and then converted back to differential energy flux and finally convolved with the SWEA energy response function. This procedure allows for direct comparison between modeled and measured electron fluxes (thick lines). Several distinct features characteristic of ionospheric primary photoelectrons [e.g. *Mitchell et al.*, 2000; *Liemohn et al.*, 2003; *Frahm et al.*, 2006a, b, 2010; *Coates et al.*, 2011; *Sakai et al.*, 2015; *Xu et al.*, 2017] are seen in the electron energy spectra. These are caused by ionization of  $\text{CO}_2$  and O by discrete features of the solar ionizing spectrum, including: (1) a cluster of peaks from 22-27 eV, corresponding to the intense 30.4-nm He-II solar line; (2) a sharp flux drop from 60 to 70 eV, corresponding to a sharp decrease of solar irradiance at wavelengths shorter than 17 nm; (3) an oxygen Auger peak near 500 eV.

Auger peaks are produced by ionization of K-shell (inner-shell) electrons of carbon, nitrogen, or oxygen atoms in  $\text{CO}_2$  and  $\text{N}_2$  by soft X-ray photons, creating electronically excited ions, which then deexcite mainly through the emission of an "Auger" electron at fixed energies [e.g. *Mitchell et al.*, 2000; *Fox et al.*, 2008; *Sakai et al.*, 2015]. The Auger electrons from the oxygen atom in  $\text{CO}_2$  create this peak near 500 eV. Carbon and nitrogen Auger peaks, with energies of  $\sim 250$  eV and  $\sim 360$  eV, respectively, are harder to identify, because  $\text{N}_2$  is not the dominant neutral species at Mars and the photoelectron flux decreases rapidly from 200 to 400 eV, which can mask the presence of a low-amplitude peak (e.g. the black thick line in Figure 2a). A small fraction of the time (0.1%), de-

excitation takes place via X-ray emission. C, N, and O K-shell (Auger) x-rays were predicted by *Cravens and Maurellis* [2001] and observed at Mars by the Chandra X-ray Observatory (CXO) [*Dennerl, 2002*], providing evidence that C, N, and O Auger processes are operating at Mars.

*Sakai et al.* [2015] hinted at the observation of C and N Auger electrons, as some of the SWEA energy spectra show sharp features at energies around 250 eV and 360 eV. For this flare event, the high photoelectron fluxes due to the enhanced short-wavelength photon irradiance provide sufficient statistics to allow for the C Auger peak in the spectra to be unequivocally identified for the first time. In Figure 2a, a bump at  $\sim 250$  eV, marked by the vertical dotted line, is seen in the post-flare spectrum (thick blue line). The flux enhancement at  $\sim 250$  eV is nine standard deviations above the baseline flux level, so it is highly unlikely to result from stochastic variability. The carbon Auger peak is also apparent in the modeled peak and post-peak spectra (Figure 2a, thin blue and red lines). During the post-flare periapsis pass, the carbon Auger peak is observed consistently for over 4 minutes. The C Auger peak can also be clearly and repeatedly identified in 6 out of 7 other flare events encountered by MAVEN.

The modeled and measured electron spectra agree to within 30% for energies below 60 eV and from 200 to 550 eV for the pre-peak and post-peak periapses (Figure 2b). Photoelectron fluxes at energies greater than  $\sim 10$  eV are roughly linearly proportional to ionizing photon fluxes [e.g. *Xu and Liemohn, 2015; Xu et al., 2015b, 2016a*]. Consequently, the modeled solar irradiance spectra are accurate for the  $\sim 17$ -60 nm and 1-6 nm wavelength ranges (the ionization potential of CO<sub>2</sub> subtracted from the photon energies),

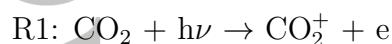
to within  $\sim 30\%$ . The larger discrepancy between modeled and observed electron fluxes between 60 and 200 eV is due to the uncertainty of the photoionization cross sections and/or the solar spectrum. Figure 2c shows the electron flux ratios of the post-peak flare and pre-peak flare periods from the SWEA data (thick) and the STET model (thin). The flux ratio agrees well below 100 eV, which suggests that the spectral irradiance model accurately predicts the solar irradiance enhancement from 11 to 60 nm between the pre-peak and post-peak periods. On the other hand, photoelectron fluxes are enhanced by up to a factor of 8 between 60 and 500 eV from the pre-peak flare period to the post-peak flare period, corresponding to the large enhancement in EUV and X-ray photons due to the flare. For the peak flare period, the photoelectron flux enhancement is a factor of  $\sim 20$  for the 200-500 eV energy range, which is consistent with a similar enhancement in the 1-2 nm solar photon flux (Figure 1a).

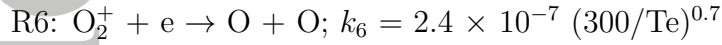
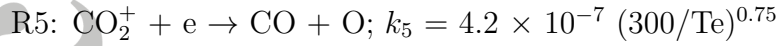
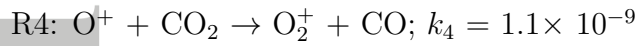
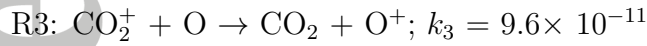
### 3. Observations and Modeling of Plasma Densities

A consequence of enhanced EUV and X-ray fluxes due to a flare event is a higher ion production rate, resulting in increased thermal plasma densities. With the STET model, we can calculate the ionization rate of  $\text{CO}_2$  (the main source for  $\text{CO}_2^+$  and  $\text{O}_2^+$ ) from photoionization (dashed) and electron impact ionization (EII, solid) for the three periods, as shown in Figure 3a. Again, for the pre-flare and peak-flare modeling, the neutral densities are taken from the pre-flare measurement while the post-peak flare case is using measurements from one orbit later. The photoionization production peak (dashed lines) is located at  $\sim 125$  km for the pre-peak flare and peak-flare periods and shifted to  $\sim 135$  km for the post-peak flare period, as the first two periods have the same neutral and  $T_e$

inputs, whereas the neutral atmosphere is expanded during the post-peak flare period. The EII production rate peaks near 120 km, 110 km, and 105 km during the pre-peak flare, post-peak-flare, and peak flare periods, respectively, corresponding with the hardness of the soft X-ray spectrum. The EII production rate exceeds the photoionization production rate below 115-120 km, even exceeding the maximum photoionization rate at the flare peak across all altitudes. Assuming a static neutral atmosphere, the total production rate is enhanced by 40% (a factor of 1.4) above 130 km and increases rapidly up to 1500% (a factor of 16) below 130 km from the pre-peak flare period to the peak flare period (red “-+-” in Figure 3b). For the post-peak flare period, the enhancement of the total production rate (blue “-+-” in Figure 3b) as a function of altitude is influenced by the neutral atmosphere expansion, in addition to the enhanced ionizing solar flux, and reaches 200% (a factor of 3) below 200 km. In particular, the enhancement for the post-peak flare period is much smaller below 105 km than for the peak-flare period, mostly because the neutral atmosphere is expanded so that X-ray photons deposit energy at a higher altitude. For the same reason, the ionization rate enhancement is greater at higher altitudes for the post-peak period than the peak-flare period.

$\text{CO}_2^+$  and  $\text{O}_2^+$  densities can be calculated by assuming photochemical equilibrium (PCE, i.e., the production rate is equal to the loss rate, and transport is negligible), which is a good approximation below 180-200 km [e.g. *Fox and Dalgarno, 1979*]. The primary reactions for the production and loss of  $\text{CO}_2^+$  and  $\text{O}_2^+$  at Mars are listed below, following *Fox and Dalgarno [1979]*.





The production rate of  $\text{CO}_2^+$  (R1) is calculated by the STET model, by summing  $\text{CO}_2$  photoionization and EII, and the rest of the reaction rates are taken from *Schunk and Nagy [2009]*. For R5 and R6, the thermal electron density is substituted with the  $\text{O}_2^+$  density, as  $\text{O}_2^+$  is the dominant ion species below 200 km. R4 is a fast reaction, so that we take the production of  $\text{O}_2^+$  being controlled by R2 and R3. A similar approach was adopted in previous studies [e.g. *Fillingim et al., 2010; Xu et al., 2016b*]. With this formalism, we obtain:

$$n(\text{CO}_2^+) = \frac{P(\text{CO}_2^+)}{(k_2 + k_3)n(\text{O}) + k_5n(\text{O}_2^+)} \quad (1)$$

$$n(\text{O}_2^+) = \sqrt{(k_2 + k_3)n(\text{CO}_2^+)n(\text{O})/k_6} \quad (2)$$

We iterate the  $\text{CO}_2^+$  and  $\text{O}_2^+$  densities with Eq. 1 and 2 until they converge to within 1% ( $\delta n/n$ ). The calculated  $\text{CO}_2^+$  and  $\text{O}_2^+$  densities are shown in Figure 3c, together with the shifted LPW thermal electron density (comparing with the dominating ion species  $\text{O}_2^+$ ) and NGIMS  $\text{CO}_2^+$  density. The pre-peak and post-peak LPW electron densities, both multiplied by the same factor of 1.4, are in good agreement with the modeled  $\text{O}_2^+$  densities, showing that the model has a similar post-peak density enhancement (relative

to the pre-flare period) to the observed one. This can be attributed to several factors: a modeled solar irradiance that is too high, uncertainties in the LPW measurements, uncertainties in the neutral densities measured by NGIMS, and uncertainties in the cross sections and reaction rates. In addition, the assumption of PCE might be less valid as MAVEN observations were made at high SZAs so that transport might be important below 180 km. Taking into account all of these uncertainties and assumptions, this 40% discrepancy between the modeled  $O_2^+$  density and the LPW electron density is reasonable.

NGIMS only measures ion profiles during alternating orbits. For the post-peak flare period, the  $CO_2^+$  density is directly taken from NGIMS measurements. For the pre-peak flare period, we use NGIMS measurements of  $CO_2^+$  densities two orbits prior to the pre-peak flare orbit, assuming the ionosphere is stable before the flare event. After multiplying by a factor of four, the  $CO_2^+$  densities measured by NGIMS have similar profiles as the modeled  $CO_2^+$  densities and exhibit a similar enhancement due to the flare. On the one hand, it indicates that the modeled  $CO_2^+$  density is roughly four times of what NGIMS measured. The measured LPW e- density is  $\sim 2$  times of the NGIMS measured  $O_2^+$  density, which might imply a factor of  $\sim 2$  absolute calibration to the NGIMS ion density. If this correction is applied to the NGIMS data, the discrepancy between the modeled and NGIMS  $CO_2^+$  densities would be within a factor of  $\sim 2$ , which might be because of the oversimplified assumption of PCE and/or other uncertainties in, such as, modeled solar irradiance. On the other hand, despite discrepancies in the absolute values, the modeled ion densities have similar altitude profiles and similar density enhancements

as the observed densities. This comparison demonstrates the validity of our approach at characterizing the relative ionospheric enhancements due to the flare event.

Below the MAVEN periapsis, the M2 (or  $O_2^+$  density) peak, is located at 125 km for the pre-peak and peak flare periods and 135 km for the post-peak flare period. For  $CO_2^+$ , the density peaks around 140-145 km for all three periods, different from that of  $O_2^+$ . As  $k_5 n(O_2^+)$  is small compared to  $(k_2 + k_3)n(O)$  (Eq. 1), the main source for  $O_2^+$  is roughly equal to  $P(CO_2^+)$ , and thus the  $O_2^+$  density peaks approximately where  $P(CO_2^+)$  peaks (Eq. 2). In contrast, the main loss of  $CO_2^+$  depends on the O density, which falls off exponentially with increasing altitude, and therefore the  $CO_2^+$  density peaks at a different altitude. Below the main peak, the  $O_2^+$  density has another small peak at 110 km for the post-peak flare period, corresponding to the EII peak in Figure 3a. Even though the peak-flare period has a maximum EII production rate at 105 km, this is more than offset by higher loss rates for  $CO_2^+$  (because of a higher O density) and  $O_2^+$  (because of a five-times smaller electron temperature) at this altitude.

Figure 3d displays the density ratios of the peak and post-peak flare periods to the pre-peak flare period. The pre-peak and peak flare periods have the same input neutral density and electron temperature profiles for the STET model so that the modeled density enhancement is entirely due to increases in solar photon fluxes. The density enhancements for  $O_2^+$  and  $CO_2^+$ , respectively, are approximately 15% and 35% above the M2 peak, becoming larger with decreasing altitude, up to 300% and  $\sim 1500\%$ . The density enhancement for  $CO_2^+$  is roughly the square of that for  $O_2^+$ , because the former is

proportional to the total production rate and the latter to the square root of the total production rate.

For the post-peak flare period, ion densities are also influenced by the neutral density and electron temperature profiles. The  $O_2^+$  density increases approximately as the square root of the ion production rate, up to  $\sim 40\%$  above 140 km and from 105 to 110 km altitude. In contrast, the  $CO_2^+$  density increases by  $\sim 40\%$  above 155 km, because of increased production (a factor of 2-3 from the blue line in Figure 3b), which is partially offset by an increased loss due to a higher O density (a factor of 1.5-2 from the magenta line in Figure 1d). Below 140 km, the  $CO_2^+$  density during the post-peak flare period is actually lower, than during the pre-peak flare period. This is because the ratio of the total production rates during the post and pre-peak flare periods is mostly less than two (blue “-+-” in Figure 3b) , while the O density is twice as high (the magenta dotted line in Figure 1d), resulting in a decreased  $CO_2^+$  density (Figures 3c-3d) because of reactions R2 and R3.

Our modeled  $O_2^+$  density profile for the post-flare period shows a clear shoulder due to the M1 peak, like some of the flare impacted electron density profiles obtained from MGS radio occultations [e.g. *Fallows et al.*, 2015c], while the pre-peak and peak-flare  $O_2^+$  density profiles lack a clear lower peak or a local minimum that would separate the M1 and M2 layers. This confirms that the separation of the M1 and M2 peaks depends on the solar spectral distribution and neutral density profiles.

#### 4. Conclusions

In this study, we investigate the low-altitude ionospheric response to the largest solar flare encountered by MAVEN to date by simulating photoelectron spectra and ion production rates and densities for the pre-peak, peak, and post-peak flare periods with the STET model. The modeled photoelectron spectra agree well with observed spectra during the pre-peak and post-peak flare periods. This agreement validates both the modeled solar EUV and soft X-ray irradiance and the STET model results above the MAVEN periapsis and gives credence to the model results below periapsis. In addition, we report the first clear identification of the carbon Auger peak in the Martian ionosphere.

Ion production rates from photoionization and electron impact ionization (EII) are obtained from STET model. By applying photochemical equilibrium, ion densities can be calculated. The background profiles for the STET model are intentionally kept the same for the pre-peak and peak flare periods so that responses to solar spectral variations can be isolated. The total production rate is found to increase by  $\sim 40\%$  for the M2 layer but up to  $200\%$  (a factor of 3) for the M1 layer. As the soft X-ray spectra become harder, the production peak for EII moves from 120 km to 105 km in altitude. Correspondingly, the  $\text{O}_2^+$  and  $\text{CO}_2^+$  densities increase, respectively, by approximately  $15\%$  and  $35\%$  above the M2 peak and by factors of up to  $300\%$  and  $\sim 1500\%$  for the M1 layer ( $\sim 100$  km altitude).

For the post-peak flare period, variations in neutral and electron temperatures due to the flare are taken into account. The production rate is enhanced by  $40\%$  to  $200\%$  above the M2 peak and  $\sim 150\%$  near the M1 peak because of a combination of increased EUV fluxes and neutral atmosphere expansion. The M2 peak is also shifted from 125 km to

135 km in altitude from the pre-peak to the post-peak flare period because of a higher  $\text{CO}_2$  density. The  $\text{O}_2^+$  density enhancement is mostly less than 50%. The loss of  $\text{CO}_2^+$  depends sensitively on the O density, which is also increased because of the flare, so that the  $\text{CO}_2^+$  density increases by less than 50% above 140 km altitude and decreases at lower altitudes.

Despite discrepancies in the absolute values, the modeled ion densities have similar altitude profiles and similar density enhancements to the observed densities, again validating our model results above the MAVEN periapsis. Below the MAVEN periapsis, the neutral density and electron temperature profiles that are used as inputs to the STET model in this study are adopted from M-GITM results, so we do not expect the calculated production rate and ion density profiles to perfectly match observations. The primary emphasis is on the relative changes from the quiet solar conditions to the flaring conditions.

**Acknowledgments.** The work was supported by the NASA MAVEN project through the Mars Exploration Program. D. Pawlowski thanks NASA for their support under grant NNX16AJ54G. The MAVEN data used in this study are available through Planetary Data System (<http://ppi.pds.nasa.gov/mission/MAVEN>). The STET simulation results for this study are available at <https://doi.org/10.6078/D1GD48>.

## References

Andersson, L., R. Ergun, G. Delory, A. Eriksson, J. Westfall, H. Reed, J. McCauly, D. Summers, and D. Meyers (2015), The Langmuir probe and waves (LPW) instrument for MAVEN, *Space Science Reviews*, 195(1-4), 173–198.

Bougher, S., D. Pawlowski, J. Bell, S. Nelli, T. McDunn, J. Murphy, M. Chizek, and A. Ridley (2015), Mars Global Ionosphere-Thermosphere Model: Solar cycle, seasonal, and diurnal variations of the Mars upper atmosphere, *Journal of Geophysical Research: Planets*, 120(2), 311–342.

Bougher, S. W., S. Engel, D. P. Hinson, and J. M. Forbes (2001), Mars Global Surveyor radio science electron density profiles : Neutral atmosphere implications, *Geophysical Research Letters*, 28, 3091–3094, doi:10.1029/2001GL012884.

Bougher, S. W., D. A. Brain, J. L. Fox, G.-G. Francisco, C. Simon-Wedlund, and P. G. Withers (2017), *Upper Neutral Atmosphere and Ionosphere*, pp. 433–463, Cambridge Planetary Science, Cambridge University Press, doi:10.1017/9781139060172.014.

Chapman, S. (1931a), The absorption and dissociative or ionizing effect of monochromatic radiation in an atmosphere on a rotating earth, *Proceedings of the Physical Society*, 43, 26–45, doi:10.1088/0959-5309/43/1/305.

Chapman, S. (1931b), The absorption and dissociative or ionizing effect of monochromatic radiation in an atmosphere on a rotating earth part II. Grazing incidence, *Proceedings of the Physical Society*, *43*, 483–501, doi:10.1088/0959-5309/43/5/302.

Coates, A. J., S. Tsang, A. Wellbrock, R. Frahm, J. Winningham, S. Barabash, R. Lundin, D. Young, and F. Crary (2011), Ionospheric photoelectrons: Comparing Venus, Earth, Mars and Titan, *Planetary and Space Science*, *59*(10), 1019–1027.

Cravens, T. E., and A. N. Maurellis (2001), X-ray emission from scattering and fluorescence of solar X-rays at Venus and Mars, *Geophysical Research Letters*, *28*(15), 3043–3046, doi:10.1029/2001GL013021.

Dennerl, K. (2002), Discovery of X-rays from Mars with Chandra, *Astronomy & Astrophysics*, *394*(3), 1119–1128.

Eparvier, F., P. Chamberlin, T. Woods, and E. Thiemann (2015), The solar extreme ultraviolet monitor for MAVEN, *Space Science Reviews*, *195*(1-4), 293–301.

Fallows, K., P. Withers, and M. Matta (2015a), Numerical simulations of the influence of solar zenith angle on properties of the M1 layer of the Mars ionosphere, *Journal of Geophysical Research: Space Physics*, *120*(8), 6707–6721, doi:10.1002/2014JA020947.

Fallows, K., P. Withers, and M. Matta (2015b), An observational study of the influence of solar zenith angle on properties of the M1 layer of the Mars ionosphere, *Journal of Geophysical Research: Space Physics*, *120*(2), 1299–1310, doi:10.1002/2014JA020750.

Fallows, K., P. Withers, and G. Gonzalez (2015c), Response of the Mars ionosphere to solar flares: Analysis of MGS radio occultation data, *Journal of Geophysical Research: Space Physics*, *120*(11), 9805–9825.

Fillington, M., L. Peticolas, R. Lillis, D. Brain, J. Halekas, D. Lummerzheim, and S. Bougher (2010), Localized ionization patches in the nighttime ionosphere of Mars and their electrodynamic consequences, *Icarus*, *206*(1), 112–119.

Fox, J. L. (1991), Cross sections and reaction rates of relevance to aeronomy, *Reviews of Geophysics*, *29*, 1110–1131.

Fox, J. L. (2004a), Advances in the aeronomy of Venus and Mars, *Advances in Space Research*, *33*(2), 132–139.

Fox, J. L. (2004b), Response of the Martian thermosphere/ionosphere to enhanced fluxes of solar soft X rays, *Journal of Geophysical Research: Space Physics*, *109*(A11).

Fox, J. L., and A. Dalgarno (1979), Ionization, luminosity, and heating of the upper atmosphere of Mars, *Journal of Geophysical Research: Space Physics (1978–2012)*, *84*(A12), 7315–7333.

Fox, J. L., and K. Sung (2001), Solar activity variations of the Venus thermosphere/ionosphere, *Journal of Geophysical Research: Space Physics*, *106*(A10), 21,305–21,335.

Fox, J. L., M. I. Galand, and R. E. Johnson (2008), Energy deposition in planetary atmospheres by charged particles and solar photons, *Space science reviews*, *139*(1-4), 3–62.

Frahm, R., J. Winningham, J. Sharber, J. Scherrer, S. Jeffers, A. Coates, D. Linder, D. Kataria, R. Lundin, S. Barabash, et al. (2006a), Carbon dioxide photoelectron energy peaks at Mars, *Icarus*, *182*(2), 371–382.

Frahm, R., J. Sharber, J. Winningham, P. Wurz, M. Liemohn, E. Kallio, M. Yamauchi, R. Lundin, S. Barabash, A. Coates, et al. (2006b), Locations of atmospheric photoelectron energy peaks within the Mars environment, *Space Science Reviews*, 126(1-4), 389–402.

Frahm, R., J. Sharber, J. Winningham, R. Link, M. Liemohn, J. Kozyra, A. Coates, D. Linder, S. Barabash, R. Lundin, et al. (2010), Estimation of the escape of photoelectrons from Mars in 2004 liberated by the ionization of carbon dioxide and atomic oxygen, *Icarus*, 206(1), 50–63.

Gurnett, D. A., D. L. Kirchner, R. L. Huff, D. D. Morgan, A. M. Persoon, T. F. Averkamp, F. Duru, E. Nielsen, A. Safaeinili, J. J. Plaut, and G. Picardi (2005), Radar Soundings of the Ionosphere of Mars, *Science*, 310, 1929–1933, doi:10.1126/science.1121868.

Haider, S., S. McKenna-Lawlor, C. Fry, R. Jain, and K. Joshipura (2012), Effects of solar X-ray flares in the E region ionosphere of Mars: First model results, *Journal of Geophysical Research: Space Physics*, 117(A5).

Haider, S., I. Batista, M. Abdu, A. Santos, S. Y. Shah, and P. Thirupathaiah (2016), Flare X-ray photochemistry of the E region ionosphere of Mars, *Journal of Geophysical Research: Space Physics*, 121(7), 6870–6888.

Haider, S. A., M. A. Abdu, I. S. Batista, J. H. Sobral, E. Kallio, W. C. Maguire, and M. I. Verigin (2009), On the responses to solar X-ray flare and coronal mass ejection in the ionospheres of Mars and Earth, *Geophysical Research Letters*, 36(13), n/a–n/a, doi:10.1029/2009GL038694, 113104.

Khazanov, G., and M. Liemohn (1995), Nonsteady state ionosphere-plasmasphere coupling of superthermal electrons, *Journal of Geophysical Research*, *100*(A6), 9669–9681.

Liemohn, M. W., D. L. Mitchell, A. F. Nagy, J. L. Fox, T. W. Reimer, and Y. Ma (2003), Comparisons of electron fluxes measured in the crustal fields at Mars by the MGS magnetometer/electron reflectometer instrument with a B field–dependent transport code, *Journal of Geophysical Research*, *108*(E12), 5134.

Lollo, A., P. Withers, K. Fallows, Z. Girazian, M. Matta, and P. C. Chamberlin (2012), Numerical simulations of the ionosphere of Mars during a solar flare, *Journal of Geophysical Research: Space Physics*, *117*(A5), n/a–n/a, doi:10.1029/2011JA017399, a05314.

Mahaffy, P. R., M. Benna, T. King, D. N. Harpold, R. Arvey, M. Barciniak, M. Bendt, D. Carrigan, T. Errigo, V. Holmes, et al. (2015), The neutral gas and ion mass spectrometer on the Mars atmosphere and volatile evolution mission, *Space Science Reviews*, *195*(1-4), 49–73.

Mahajan, K., N. K. Lodhi, and S. Singh (2009), Ionospheric effects of solar flares at Mars, *Geophysical Research Letters*, *36*(15).

Mendillo, M., P. Withers, D. Hinson, H. Rishbeth, and B. Reinisch (2006), Effects of solar flares on the ionosphere of Mars, *Science*, *311*(5764), 1135–1138.

Mendillo, M., A. Lollo, P. Withers, M. Matta, M. Ptzold, and S. Tellmann (2011), Modeling Mars' ionosphere with constraints from same-day observations by Mars Global Surveyor and Mars Express, *Journal of Geophysical Research: Space Physics*, *116*(A11), n/a–n/a, doi:10.1029/2011JA016865, a11303.

Mitchell, D., R. Lin, H. Reme, D. Crider, P. Cloutier, J. Connerney, M. Acuña, and N. Ness (2000), Oxygen Auger electrons observed in Mars' ionosphere, *Geophysical research letters*, 27(13), 1871–1874.

Mitchell, D., C. Mazelle, J.-A. Sauvaud, J.-J. Thocaven, J. Rouzaud, A. Fedorov, P. Rouger, D. Toubanc, E. Taylor, D. Gordon, et al. (2016), The MAVEN solar wind electron analyzer, *Space Science Reviews*, 200(1-4), 495–528.

Nielsen, E., H. Zou, D. Gurnett, D. Kirchner, D. Morgan, R. Huff, R. Orosei, A. Safaeinili, J. Plaut, and G. Picardi (2007), Observations of vertical reflections from the topside Martian ionosphere, in *The Mars plasma environment*, pp. 373–388, Springer.

Peterson, W., T. Woods, J. Fontenla, P. Richards, P. Chamberlin, S. Solomon, W. Tobiska, and H. Warren (2012), Solar EUV and XUV energy input to thermosphere on solar rotation time scales derived from photoelectron observations, *Journal of Geophysical Research: Space Physics* (1978–2012), 117(A5).

Peterson, W., E. Thiemann, F. G. Eparvier, L. Andersson, C. Fowler, D. Larson, D. Mitchell, C. Mazelle, J. Fontenla, J. S. Evans, et al. (2016), Photoelectrons and solar ionizing radiation at Mars: Predictions versus MAVEN observations, *Journal of Geophysical Research: Space Physics*, 121(9), 8859–8870.

Qian, L., A. G. Burns, P. C. Chamberlin, and S. C. Solomon (2011), Variability of thermosphere and ionosphere responses to solar flares, *Journal of Geophysical Research: Space Physics*, 116(A10).

Sakai, S., A. Rahmati, D. L. Mitchell, T. E. Cravens, S. W. Bougher, C. Mazelle, W. K. Peterson, F. G. Eparvier, J. M. Fontenla, and B. M. Jakosky (2015), Model insights into

energetic photoelectrons measured at Mars by MAVEN, *Geophysical Research Letters*, 42(21), 8894–8900, doi:10.1002/2015GL065169, 2015GL065169.

Schunk, R., and A. Nagy (2009), *Ionospheres*, Cambridge University Press.

Thiemann, E. M. B., F. G. Eparvier, L. A. Andersson, C. M. Fowler, W. K. Peterson, P. R. Mahaffy, S. L. England, D. E. Larson, D. Y. Lo, N. M. Schneider, J. I. Deighan, W. E. McClintock, and B. M. Jakosky (2015), Neutral density response to solar flares at Mars, *Geophysical Research Letters*, 42(21), 8986–8992, doi:10.1002/2015GL066334, 2015GL066334.

Thiemann, E. M. B., L. Andersson, R. Lillis, P. Withers, S. Xu, M. Elrod, S. Jain, M. D. Pilinski, D. Pawlowski, P. C. Chamberlin, F. G. Eparvier, M. Benna, C. Fowler, S. Curry, and W. K. Peterson (2018), The Mars Topside Ionosphere Response to the X8.2 Solar Flare of 10 September 2017, *Geophysical Research Letters*, 45, in press, doi:10.1029/2018GL077730.

Withers, P. (2009), A review of observed variability in the dayside ionosphere of Mars, *Advances in Space Research*, 44, 277–307, doi:10.1016/j.asr.2009.04.027.

Xu, S., and M. W. Liemohn (2015), Superthermal electron transport model for Mars, *Earth and Space Science*, 2(3), 47–64, doi:10.1002/2014EA000043, 2014EA000043.

Xu, S., M. W. Liemohn, W. Peterson, J. Fontenla, and P. Chamberlin (2015a), Comparison of different solar irradiance models for the superthermal electron transport model for Mars, *Planetary and Space Science*, 119, 62–68.

Xu, S., M. Liemohn, S. Bougher, and D. Mitchell (2015b), Enhanced carbon dioxide causing the dust storm-related increase in high-altitude photoelectron fluxes at Mars,

*Geophysical Research Letters*, 42(22), 9702–9710.

Xu, S., M. Liemohn, S. Bougher, and D. Mitchell (2016a), Martian high-altitude photoelectrons independent of solar zenith angle, *Journal of Geophysical Research: Space Physics*, 121(4), 3767–3780, doi:10.1002/2015JA022149, 2015JA022149.

Xu, S., D. Mitchell, M. Liemohn, C. Dong, S. Bougher, M. Fillingim, R. Lillis, J. McFadden, C. Mazelle, J. Connerney, and B. Jakosky (2016b), Deep nightside photoelectron observations by MAVEN SWEA: Implications for Martian northern hemispheric magnetic topology and nightside ionosphere source, *Geophysical Research Letters*, 43(17), 8876–8884, doi:10.1002/2016GL070527, 2016GL070527.

Xu, S., D. Mitchell, M. Liemohn, X. Fang, Y. Ma, J. Luhmann, D. Brain, M. Steckiewicz, C. Mazelle, J. Connerney, and B. Jakosky (2017), Martian low-altitude magnetic topology deduced from MAVEN/SWEA observations, *Journal of Geophysical Research: Space Physics*, pp. n/a–n/a, doi:10.1002/2016JA023467, 2016JA023467.

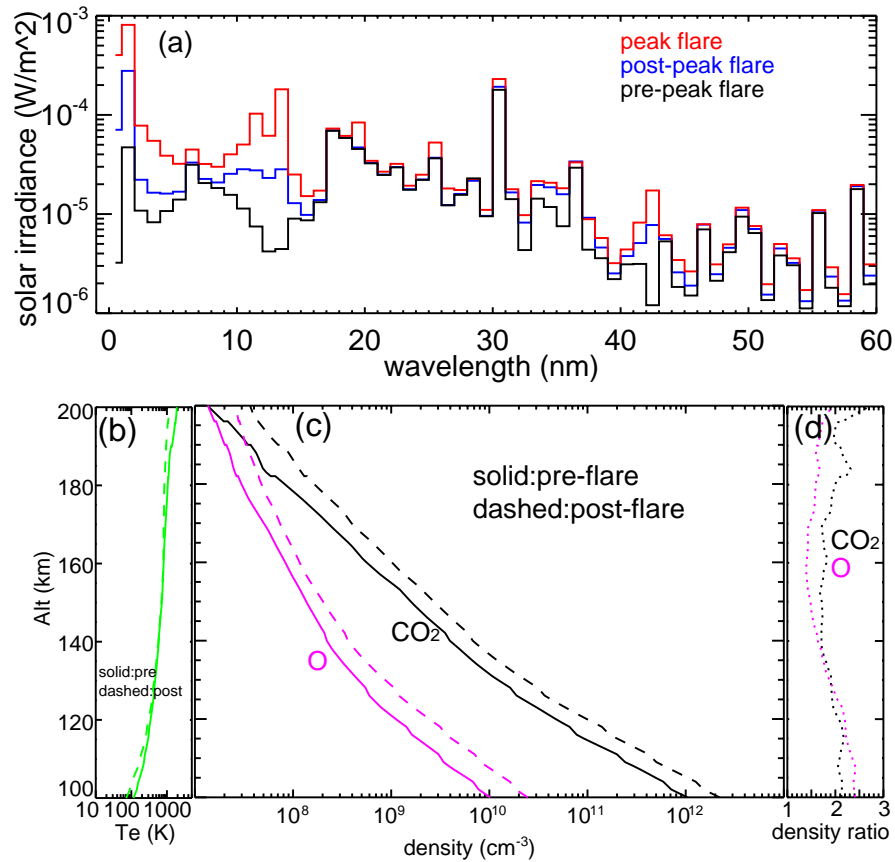


**Figure 1.** (a) Solar irradiance for 0.1–60 nm from a spectral irradiance model [*Thiemann et al.*, 2018] for the three periods. (b) Electron temperature profiles for the pre-peak flare (solid) and post-peak flare (dashed) periods. (c) Profiles of the CO<sub>2</sub> density (black) and the O density (magenta) for the pre-peak flare (solid) and post-peak flare (dashed) periods. (d) The density ratio of the post-peak flare and pre-peak flare periods for CO<sub>2</sub> (black) and O (magenta). The pre-peak flare profiles are used to model the peak-flare period as well.

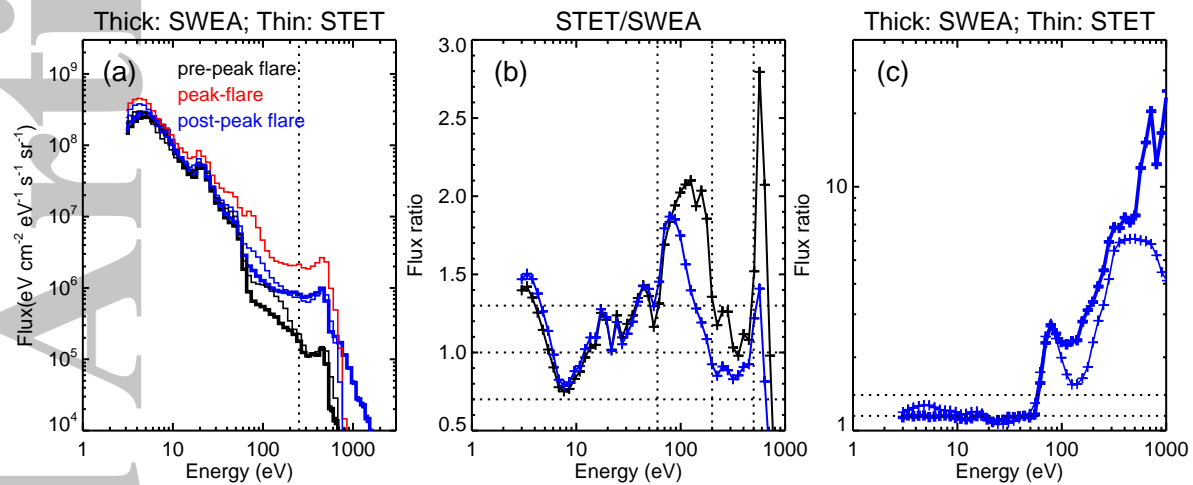


**Figure 2.** (a) The modeled photoelectron spectra at 155 km for the three periods are shown as thin lines in different colors. Overplotted as the black and blue thick lines are observed photoelectron spectra from SWEA at 155 km for the pre-peak flare and post-peak flare periods, respectively. (b) STET modeled electron fluxes divided by the measured electron fluxes for the post-peak flare (blue) and pre-peak flare (black) periods. (c) The electron flux ratio of the post-peak flare and pre-peak flare periods, the blue lines divided by the black lines in (a), from the SWEA data (thick) and STET model results (thin).

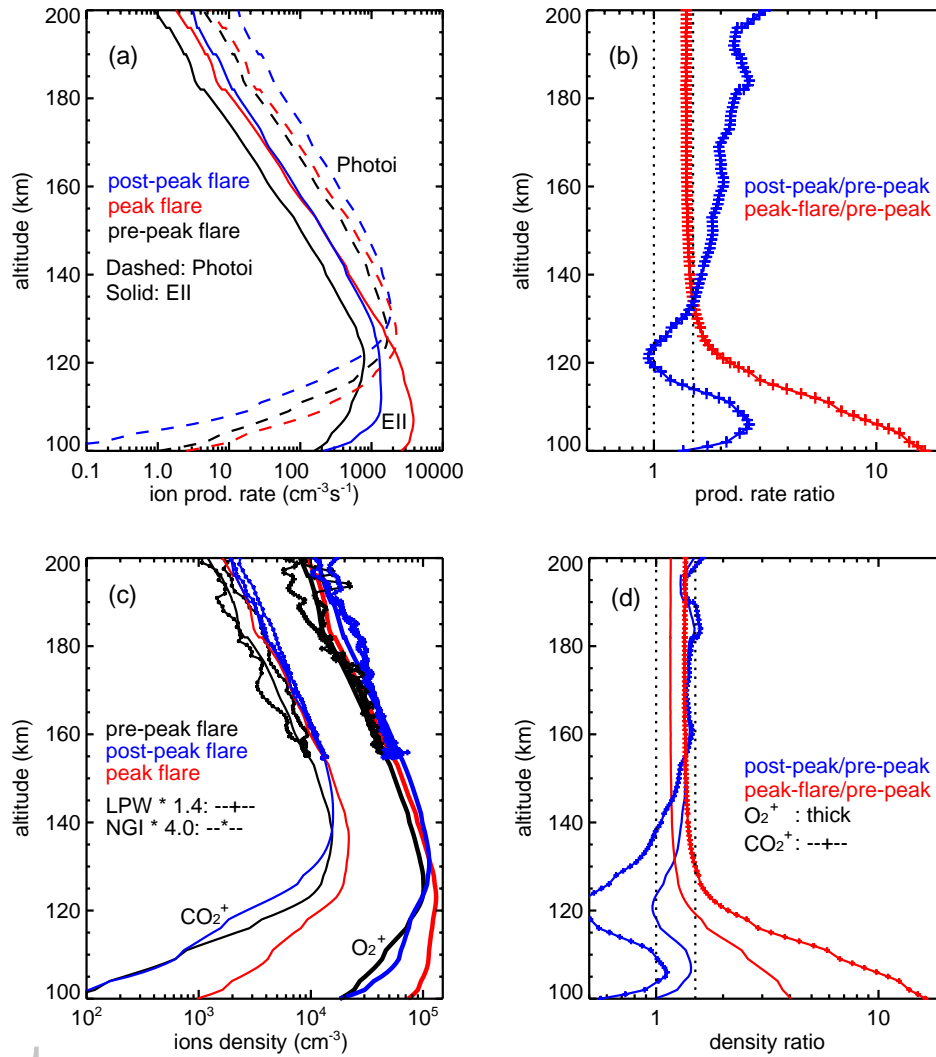


**Figure 3.** (a) The ion production rate of  $\text{CO}_2^+$  from photoionization (dashed) and EII (solid) for the three periods. (b) The total production rates (photoionization + EII) of the peak-flare and post-peak flare periods are divided by that of the pre-peak flare period, colored in blue and red, respectively. (c) Profiles of  $\text{CO}_2^+$  (thin solid lines) and  $\text{O}_2^+$  (thick solid lines) densities for the three periods, highlighted in different colors. Thermal electron densities from LPW (multiplied by a factor of 1.4) and  $\text{CO}_2^+$  densities from NGIMS (multiplied by a factor of 4) are plotted over as ‘-+-’ and ‘-\*-\*’, respectively, for inbound and outbound of the pre-peak flare (black) and post-peak flare (blue) orbits. (d) The density ratio of  $\text{CO}_2^+$  (‘-+-’) and  $\text{O}_2^+$  (thick solid lines) for the peak-flare and post-peak flare periods divided by that of the pre-peak flare period, colored in blue and red, respectively. The vertical dotted lines in (b) and (d) mark values of 1 and 1.5.